Research Article

New two-layer Ruddlesden–Popper cathode materials for protonic ceramics fuel cells

Yihan LING[*], Tianming GUO, Yangyang GUO, Yang YANG, Yunfeng TIAN, Xinxin WANG, Xuemei OU, Peizhong FENG

School of Materials Science and Physics, China University of Mining and Technology, Xuzhou 221116, China

Abstract: New two-layer Ruddlesden–Popper (RP) oxide $La_{0.25}Sr_{2.75}FeNiO_{7-\delta}$ (LSFN) in the combination of $Sr_3Fe_2O_{7-\delta}$ and $La_3Ni_2O_{7-\delta}$ was successfully synthesized and studied as the potential active single-phase and composite cathode for protonic ceramics fuel cells (PCFCs). LSFN with the tetragonal symmetrical structure (*I*4/*mmm*) is confirmed, and the co-existence of Fe^{3+}/Fe^{4+} and Ni^{3+}/Ni^{2+} couples is demonstrated by X-ray photoelectron spectrometer (XPS) analysis. The LSFN conductivity is apparently enhanced after Ni doping in Fe-site, and nearly three times those of $Sr_3Fe_2O_{7-\delta}$, which is directly related to the carrier concentration and conductor mechanism. Importantly, anode supported PCFCs using $LSFN–BaZr_{0.1}Ce_{0.7}Y_{0.2}O_{3-\delta}$ (LSFN–BZCY) composite cathode achieved high power density (426 mW·cm^{-2} at 650 ℃) and low electrode interface polarization resistance (0.26 Ω·cm^2). Besides, distribution of relaxation time (DRT) function technology was further used to analyse the electrode polarization processes. The observed three peaks (P1, P2, and P3) separated by DRT shifted to the high frequency region with the decreasing temperature, suggesting that the charge transfer at the electrode–electrolyte interfaces becomes more difficult at reduced temperatures. Preliminary results demonstrate that new two-layer RP phase LSFN can be a promising cathode candidate for PCFCs.

Keywords: protonic ceramics fuel cells (PCFCs); Ruddlesden–Popper (RP) phase; single-phase cathode; distribution of relaxation time (DRT) function; charge transfer

1 Introduction

Protonic ceramics fuel cells (PCFCs) possess several advantages of high proton conductivity electrolytes with low activation energy and high fuel efficiency, being more attractive at reduced operating temperatures [1–4]. However, as the temperature reduced, the corresponding challenge for the oxygen reduction reaction is the reduced cathodic catalytic activity, causing the large electrode polarization loss and fast degradation of cell performance [5–7]. Therefore, great efforts have been devoted to developing new cathode materials and modifying high performance conventional cathode materials that can own high catalytic activity at reduced temperatures.

New cathodes with mixed conductivity based on simple perovskite (doped $LaCoO_3$, $BaCoO_3$, and $LaFeO_3$) have been extensively studied [8–13]. Considering high oxygen-ion defect concentration, oxygen diffusion

* Corresponding author.
E-mail: lyhyy@cumt.edu.cn

anisotropy, and cation ordered-structure, several recent studies have highlighted the promising of the Ruddlesden–Popper (RP) series, $A_{n+1}BnO_{3n+1}$, for cathode application, where the special sandwich structure consists of n ABO_3 perovskite and two AO rock salt layers [14–19]. The $Sr_3Fe_2O_{7-\delta}$-based systems, belonging to the $n = 2$ series, have been widely investigated owing to their high oxygen deficiency, excellent water-intercalation property, and prominent catalytic activity [20–22]. The partial substitution of Ni for Fe in $Sr_3Fe_2O_{7-\delta}$ can increase the electrical conductivity and the oxygen permeability without structural transformation [23,24]. In our previous works, the introduction of La into Sr-site forming $La_xSr_{3-x}Fe_2O_{7-\delta}$ can enhance thermo-chemical stability as well as large oxygen deficiency [25,26]. Moreover, another RP phase, $La_3Ni_2O_{7-\delta}$ ($n = 2$), showed large electrical conductivity, acceptable stability, and similar thermal expansion coefficient to electrolytes [27–29]. Therefore, in this work, we combine the advantages of $Sr_3Fe_2O_{7-\delta}$ and $La_3Ni_2O_{7-\delta}$ RP phase oxides thanks to their similar ionic radii and chemical properties, expecting to enhance the conductivity and electrochemical activity without structural transformation. Here, $La_{0.25}Sr_{2.75}FeNiO_{7-\delta}$ (LSFN) was successfully prepared and the electrochemical performance was investigated to verify the possibility for using as cathode material for PCFCs. In addition, LSFN incorporated with $BaZr_{0.1}Ce_{0.7}Y_{0.2}O_{3-\delta}$ (BZCY) to form a composite cathode for PCFCs was also examined. The polarization processes for PCFCs under working condition were detailly analyzed by the distribution of relaxation time (DRT) method.

2   Experimental

LSFN, NiO–BZCY, and BZCY powders were synthesized by ethylenediamine tetraacetic acid (EDTA)–citric acid combustion method, and the primary powders were calcined at 1200, 1100, and 1100 ℃ for 3 h, respectively [30]. X-ray diffraction (XRD) was used to perform all prepared powders as well as LSFN–BZCY (1:1 wt%) mixtures calcined at different temperatures. X-ray photoelectron spectrometer (XPS) was used to analyze the elemental chemical state of LSFN, and then the conductivity measurement by H.P. multimeter using the standard DC four-probe technique was investigated from 800 to 300 ℃ in air.

Anode supported PCFCs with LSFN single-phase and composite cathode was used to investigate the electrochemical performance. The NiO–BZCY-starch/ NiO–BZCY/BZCY anode supported half cells were prepared by the dry pressing and then sintering at 1400 ℃ for 3 h. Finally, LSFN and LSFN–BZCY (7:3 wt%) cathode slurries were brushed onto BZCY electrolyte surface severally, and then calcined at 900 ℃ for 3 h in air. The effective electrode area of the single cells was 0.2 cm². Anode supported PCFCs were evaluated by cell-testing system with humidified (~3% H_2O) H_2 fuel at 500–650 ℃. The impedance spectra (Chi604E, Shanghai Chenhua) under open-current conditions were investigated with the frequency range of 0.01 Hz–100 kHz and AC amplitude of 10 mV at 500–650 ℃, of which the microstructure was performed using scanning electron microscopy (SEM).

3   Results and discussion

XRD pattern of prepared LSFN powder is presented in Fig. 1(a), which clearly shows the tetragonal symmetry defined with the space group of *I*4/*mmm* in the light of standard powder diffraction information for $Sr_3Fe_2O_{7-\delta}$, indicating that the partial replacement of Fe with Ni can not affect the single RP phase structure [20–22]. Rietveld analysis was performed by the GSAS software and the XRD Rietveld refinement results are also given in Figs. 1(a) and 1(b) (the magnified results with 2θ of 25°–50°), where low refinement reliability factors ($w_{Rp} =$ 12.90%, R_p = 9.84%, and χ^2 = 2.05) were obtained. The calculated lattice parameters a and c based on this model are 3.8364(50) and 20.0376(93) Å, respectively, and one can clearly see that two perovskite layers are sandwiched by the rock-salt layer along the c-axis in the typical two-layer RP phase structure as illustrated in Fig. 1(c). In addition, LSFN sample with high crystallinity and well-defined crystalline fringes was observed in Fig. 1(d), and the lattice spacing of 0.2658 nm corresponds to the lattice spacing of the (110) plane in the tetragonal symmetry in selected- angle diffraction in Fig. 1(b). All results together demonstrate the well maintained single RP phase structure after the combination of two RP phase oxides of $Sr_3Fe_2O_{7-\delta}$ and $La_3Ni_2O_{7-\delta}.$

The elemental chemical state was characterized by XPS, and La 3d, Sr 3d, Fe 2p, and Ni 2p peaks in XPS spectra for LSFN sample at room temperature are shown in Fig. 2. The peaks of binding energies of La
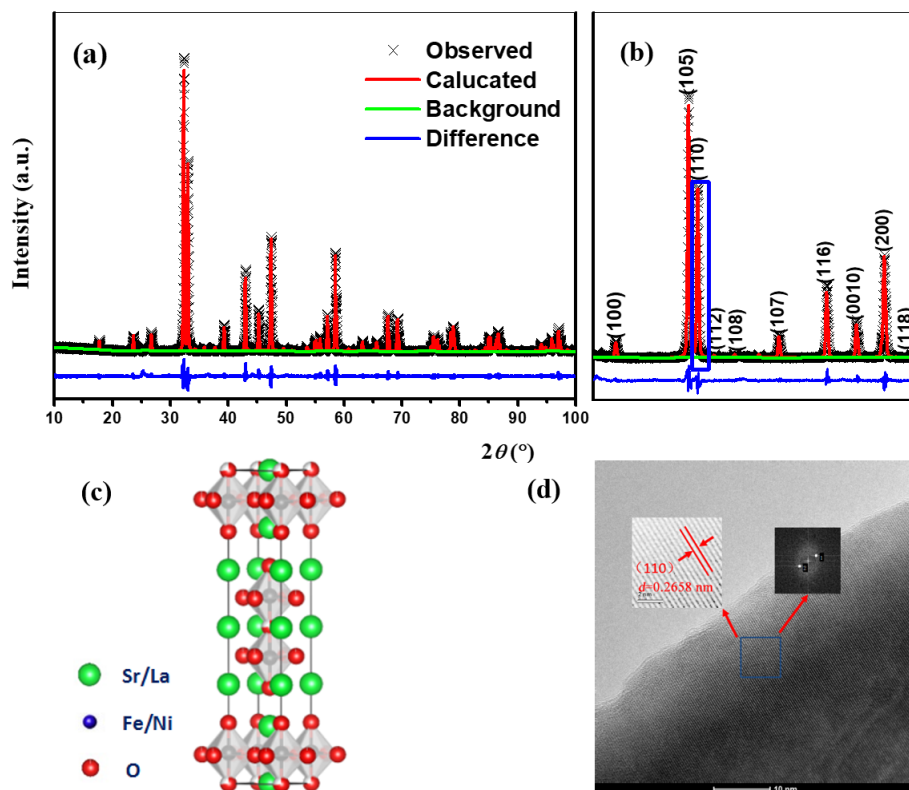
Fig. 1 (a) Rietveld refinement data for LSFN powder prepared through EDTA–citric acid combustion method, and calcined at 1200 ℃ for 3 h; (b) magnified results with 2θ of 25°–50°; (c) the typical two-layer RP phase structure; and (d) high-resolution TEM image of LSFN samples.
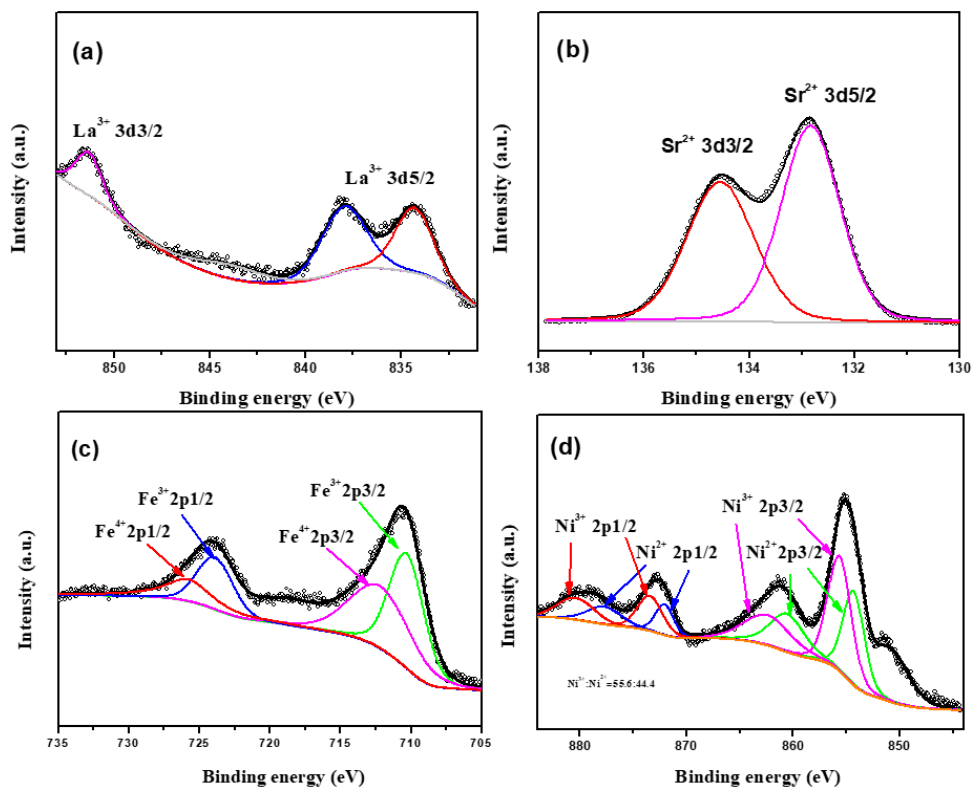
Fig. 2 XPS spectra at room temperature for (a) La 3d, (b) Sr 3d, (c) Fe 2p, and (d) Ni 2p of LSFN sample.

3d5/2 (at 834.4 and 838.1 eV) and La 3d3/2 (at 851.5 eV) represent La^{3+} as revealed in Fig. 2(a). Figure 2(b) proves Sr in LSFN sample displays a 2^+ valence state with the binding energies of Sr 3d5/2 (at 132.8 eV) and Sr 3d 3/2 (at 134.6 eV). Figure 2(c) shows the Fe 2p binding energy region of LSFN sample, where the location of 710.5/724.1 eV and 712.5/725.9 eV peaks are related to the (Fe 2p3/2)/(Fe 2p1/2) signals for Fe^{3+} and Fe^{4+}, respectively, and the proportion of Fe^{4+}/Fe^{3+} is about 0.898 without the peaks of Fe^{2+} [31,32]. Figure 2(d) reports the Ni 2p XPS spectra of LSFN sample, and the Ni 2p peaks that envelope the Ni^{2+} and Ni^{3+} valence states are fitted. One can clearly observe the four characteristic peaks with the binding energy of 855.8, 862.7, 873.5, and 880.5 eV, which related to Ni^{3+} 3d5/2 and Ni^{3+} 3d3/2, while the peaks of 2p1/2 at 872.1 and 877.8 eV and 2p3/2 at 854.4 and 860.7 eV can be attributed to Ni^{2+}, where the proportion of Ni^{3+}/Ni^{2+} is about 1.25 [33–35]. The XPS results conform the fact that Fe^{3+}/Fe^{4+} and Ni^{3+}/Ni^{2+} couples co-exist in the LSFN sample. Moreover, the conductivity of LSFN can be considered to be affected in LSFN sample as follows:

$$Fe^{4+} + Ni^{2+} \leftrightarrow Fe^{3+} + Ni^{3+} \qquad (1)$$
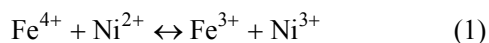
Therefore, the introduction Ni^{3+}/Ni^{2+} couples would be expected to enhance the conductivity and electrochemical properties of the LSFN sample.

The electrical conductivity for $Sr_3Fe_2O_{7-\delta}$ sample increases to a peak of about 60.4 $S \cdot cm^{-1}$ at around 500 ℃, and then reduces as the temperature increases from 300 to 800 ℃ as shown in Fig. 3, exhibiting typical semi-conductor-like behavior [21,22]. Figure 3 also gives the electronic conductivity of LSFN sample
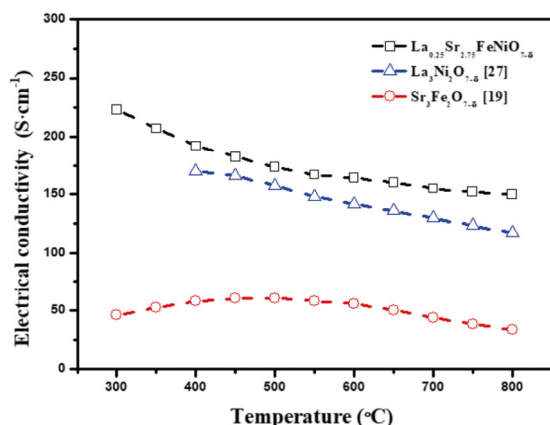
measured at 300–800 ℃ in air, and LSFN sample presents typical metallic behavior as well as $La_3Ni_2O_{7-\delta}$, of which the conductivities increase with the decrease of temperatures (223 $S \cdot cm^{-1}$ at 300 ℃ [29]). The charge carriers, Fe^{3+}/Fe^{4+} and Ni^{3+}/Ni^{2+} redox couples, directly affect the change from the semiconductor-like to metallic conducting behavior, indicating that Ni doping into Fe-site causes the 3d electron delocalized [23,34]. Therefore, LSFN sample presents improved conductivity and is superior to both $Sr_3Fe_2O_{7-\delta}$ and $La_3Ni_2O_{7-\delta}$.

Before the electrochemical performance of LSFN single-phase and composite cathode for anode supported PCFCs was measured, the chemical compatibility behavior of LSFN–BZCY mixture was evaluated. LSFN–BZCY mixture with the same mass was calcined in air at 800–1100 ℃ for 10 h. There is no reaction between LSFN and BZCY before 1000 ℃ as shown in Fig. 4. Although a small amount of $(BaSr)FeO_{3-\delta}$ was observed, the vast majority of the LSFN–BZCY composite was very stable after calcined at 1100 ℃. Meanwhile, $(BaSr)FeO_{3-\delta}$-based cathode owns high catalytic activity and exhibits excellent electrochemical performance (696 $mW \cdot cm^{-2}$ at 700 ℃ [36]). Therefore, anode supported PCFCs based on LSFN single-phase and composite cathode have been measured from 650 to 500 ℃, and I (current density)–V (voltage)–P (power density) curves are given in Fig. 5. The open-circuit voltage values of LSFN and LSFN–BZCY at 650 ℃ are 1.02 and 1.04 V, respectively, indicating the highly dense microstructure of BZCY electrolyte. The maximum power densities of LSFN single-phase cathode are 348.0, 219.6, 136.2, and 71.7 $mW \cdot cm^{-2}$ at 650, 600, 550, and 500 ℃, respectively. In order to

Fig. 3 Temperature dependence on conductivity for LSFN in air, and $Sr_3Fe_2O_{7-\delta}$ and $La_3Ni_2O_{7-\delta}$ conductivity data from Refs. [19,27].

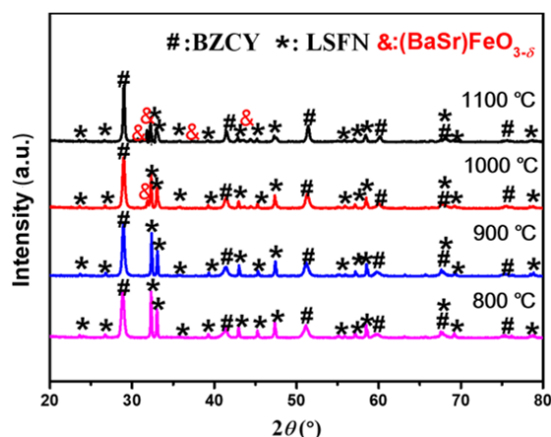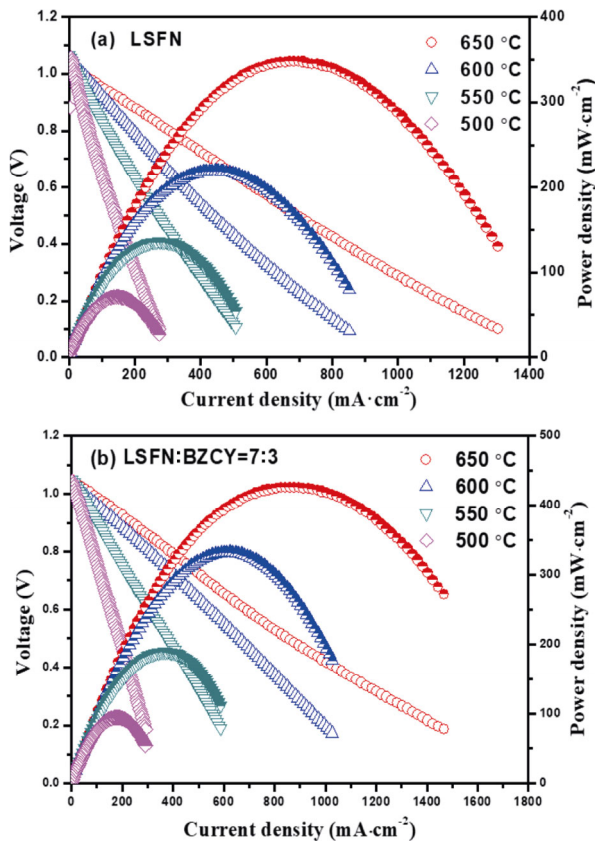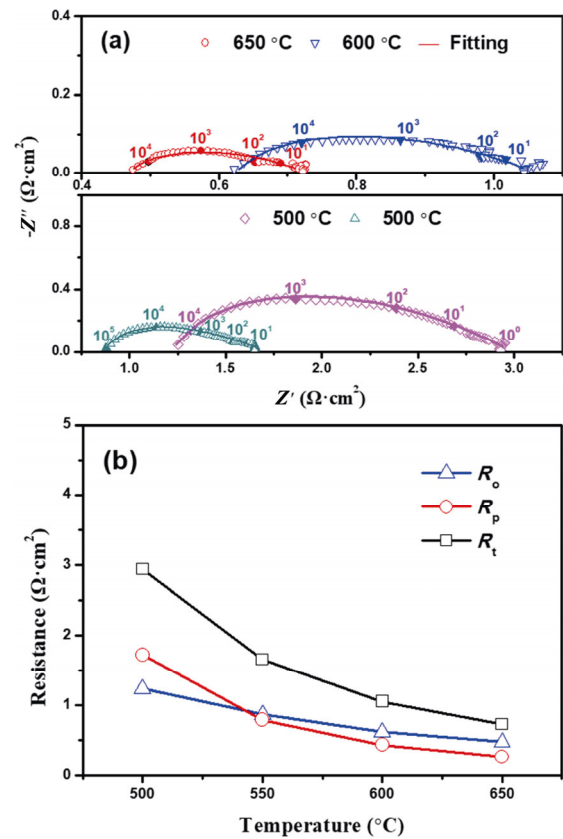**Fig. 4** XRD patterns of LSFN–BZCY mixture calcined at 800–1100 ℃ for 10 h.

Fig. 5 (a) *I–V–P* curves of anode supported PCFCs with LSFN single-phase cathode and (b) LSFN–BZCY composite cathode measured from 650 to 500 ℃.

Fig. 6 (a) Impedance spectra for anode supported PCFCs with LSFN–BZCY composite cathode measured under open-circuit conditions from 650 to 500 ℃, and (b) the temperature dependence of electrode interfacial polarization resistance (R_p), ohmic resistance (R_o), and total resistance (R_t).

determine the cell performance of the optimal mixing ratio of LSFN and BZCY, the detailed *I–V–P* curves are shown in Figs. S1–S3 in the Electronic Supplementary Material (ESM). Considering the same single cell structure and the same fabrication technology, the performance of single cell is directly attributed to the electrochemical behaviors of cathodes. This result indicates that the single cell using LSFN–BZCY (7:3) composite cathode as cathode exhibits a better performance. Obviously, LSFN–BZCY composite cathode exhibits much higher performance than Co-doped $La_3Ni_2O_{7-\delta}$ (398 mW·cm^{-2} [29]), but is still lower than $Sr_3Fe_2O_{7-\delta}$–5 wt%BZCY composite cathode (583 mW·cm^{-2} [21]).

To evaluate the catalytic performance of LSFN–BZCY composite cathode for oxygen reduction reactions, electrochemical impedance spectroscopy (EIS) measurements were used to perform anode supported PCFCs under open-circuit conditions as shown in Fig. 6(a). Electrode polarization resistance (R_p) and the ohmic resistance (R_o) can be calculated from the impedance as well as the total resistance (R_t), and then presented

in Fig. 6(b). Temperature has a significant effect on R_p and R_o at the working temperatures, and the R_p value increased from 0.26 to 1.72 Ω·cm^2 with reducing the temperature, while corresponding R_o only changes from 0.47 to 1.23 Ω·cm^2, indicating that the R_p is the rate-limiting step for PCFCs at low temperatures. LSFN–BZCY composite cathode exhibits low R_p than Co-doped $La_3Ni_2O_{7-\delta}$ (7.6 Ω·cm^2 [29]), but much larger than $Sr_3Fe_2O_{7-\delta}$–5 wt%BZCY composite cathode (0.15 Ω·cm^2 [21]).

As to further detailly investigate the electrode polarization process of anode supported PCFCs with LSFN composite cathode under open circuit voltage (OCV) conditions, the impedance spectrum analysis using the DRT method can be characterized as the peaks in the $F(\tau)$ vs. $-\log_{10}(2\pi\tau)$ curves as follows [37–40]:

$$F(\tau) = \tau G(\tau)\ln(10)$$

$$= \frac{-\ln(10)}{\pi}\left[Z''\left(e^{-\ln\tau+\frac{j\pi}{2}}\right) + Z''\left(e^{-\ln\tau-\frac{j\pi}{2}}\right)\right] \quad (2)$$

where Z'' refers to the imaginary part of Z; τ is the relaxation time related to the frequency f according to $\tau = 1/2\pi f$. As shown in Fig. 7(a), the calculated DRT plots exhibit several polarization processes. It clearly can be seen that there exist three (P1, P2, and P3) main peaks at different operation temperatures, suggesting there are three rate-limiting steps. Meanwhile, all the peaks shift to high frequencies with reducing the temperatures, suggesting the charge transfer with electron and oxygen-ion at reduced temperatures becomes more difficult at the electrode–electrolyte interfaces. Simulated resistances corresponded to P1, P2, and P3 are presented in Figs. 7(b) and 7(c). P1 observed at the high frequency decreases with the increasing temperature, and therefore P1 is considered to be proton incorporation and diffusion at cathode–electrolyte interface [38,39]. As can be seen from Fig. 7(b), the proportion of P1 is much larger than those of P2 and P3, indicating that P1 is the rate-limiting step for the reaction. The DRT result of LSFN at 650 ℃ as a comparison is shown in Fig. S4 in the ESM. It can be seen that LSFN also has P1 peak concerning proton transmission with the proton conductivity of LSFN. However, through the analysis at the same temperature, the proportion of P1 in the

results of composite BZCY is significantly higher than that of non-composite BZCY. Since LSFN single-phase cathode has ignorable proton conductivity, the mixure of BZCY can dramatically improve the proton conducting behavior. P2 is the process of H_2 adsorption, dissociation, and proton formation at anode, and the proportion of P2 is almost the same as temperature reduced. Certainly, P3 also decreases with the increasing temperature and locates at the low frequencies. Therefore, P3 is supposed to oxygen dissociation, adsorption, and diffusion in cathode with low proportion of about 19 % at 500 ℃ owing to excellent conductivity of LSFN.

Figure 8 shows the long-term stability test of LSFN composite cathode with a 500 mA·cm^{-2} discharge current density at 650 ℃ in humidified H_2 fuel. The output voltages varied with test time were recorded, and the results indicated that the voltage remained a stable value at 0.73 V within 220 h test. Figure 9(a) shows cross-sectional images of anode supported PFCFs with LSFN–BZCY cathode after long-term testing. The 30 μm-thickness proton BZCY electrolyte is dense enough and adheres well with LSFN–BZCY cathode under the cover of silver, preventing the gas leakage and ensuring efficient proton transmission.
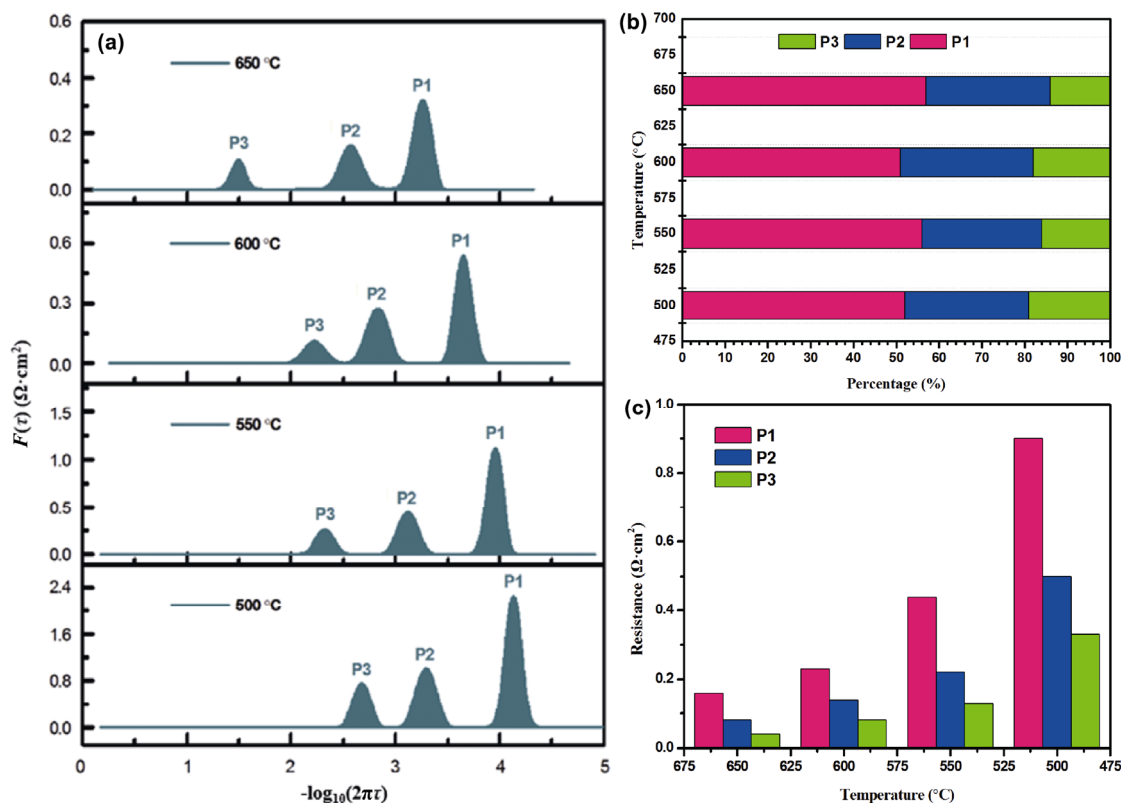
Fig. 7 (a) DRT analysis results of the impedance spectra under open-circuit conditions from 650 to 500 ℃, and (b, c) simulated resistances of P1, P2, and P3 corresponding to each fitted peak.
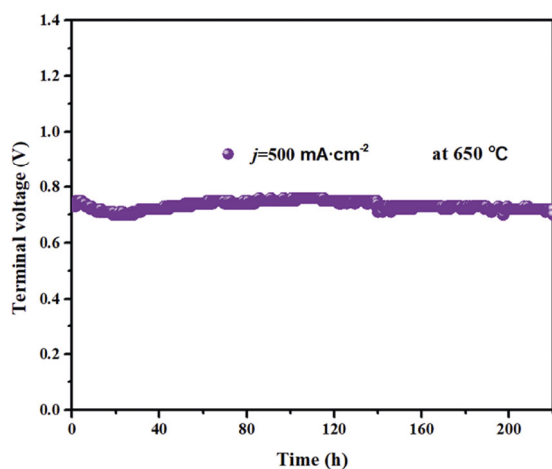
Fig. 8 Long-term stability of anode supported PCFCs with LSFN–BZCY composite cathode with the applied discharge current density of 500 mA·cm^{-2} at 650 ℃.
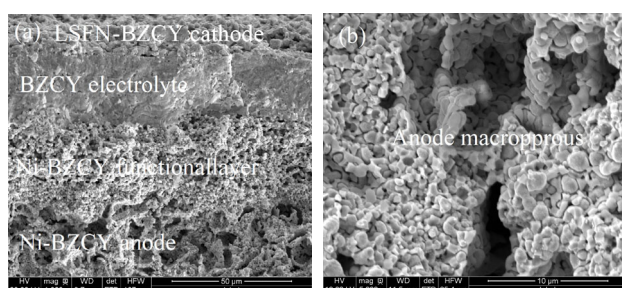
Fig. 9 SEM images of anode supported PCFCs with LSFN–BZCY cathode: (a) cross-section and (b) Ni–BZCY anode substrate.

Besides, there are many micropores at the approximate 35 μm-thick anode functional layer from the reduction of NiO and macroporous at anode substrate as shown in Fig. 9(b), leading to a better interfacial contact between anode substrate and electrolyte. Preliminary results demonstrated that new two-layer RP structure LSFN must be a promising cathode candidate for PCFCs, and catalytic activity and proton conductivity of LSFN single-phase cathode can be further enhanced by incorporation with BZCY.

4　Conclusions

In this work, we successfully synthesized two-layer RP oxide LSFN and then it was evaluated as the active single-phase and composite cathode for PCFCs. LSFN with the tetragonal symmetrical structure (*I*4/*mmm*) is confirmed by the XRD Rietveld refinement. Furthermore, the XPS results obviously prove the co-existence of Fe^{3+}/Fe^{4+} and Ni^{3+}/Ni^{2+} couples in the combination of

two RP phase oxides of $Sr_3Fe_2O_{7-\delta}$ and $La_3Ni_2O_{7-\delta}$, and directly affect the change from the semiconductor-like to metallic conducting behavior confirmed by the conductivity measurement. Importantly, anode supported PCFCs using LSFN–BZCY cathode achieved maximum power densities of 426.0, 332.3, 188.8, and 94.5 mW·cm^{-2} from 650 to 500 ℃, with corresponding R_p of 0.29, 0.43, 0.79, and 1.72 Ω·cm^2, respectively. The electrode polarization processes were further analyzed using the DRT function, and thus three polarization peaks (P1, P2, and P3) observed in DRT curves shifted to the right at high frequencies with decreasing the temperature, suggesting that the charge transfer at the electrode–electrolyte interfaces becomes more difficult at reduced temperatures. Preliminary results demonstrated two-layer RP structured LSFN can be a promising cathode candidate for PCFCs.

Electronic Supplementary Material

Supplementary material is available in the online version of this article at https://doi.org/10.1007/s40145-021-0488-8.

References

[1] Radenahmad N, Afif A, Petra PI, *et al*. Proton-conducting electrolytes for direct methanol and direct urea fuel cells–A state-of-the-art review. *Renew Sustain Energy Rev* 2016, **57**: 1347–1358.

[2] Duan CC, Kee RJ, Zhu HY, *et al*. Highly durable, coking and sulfur tolerant, fuel-flexible protonic ceramic fuel cells. *Nature* 2018, **557**: 217–222.

[3] Bonanos N, Huijser A, Poulsen FW. H/D isotope effects in high temperature proton conductors. *Solid State Ion* 2015, **275**: 9–13.

[4] Wang XX, Wei KW, Yan SL, *et al*. Efficient and stable conversion of oxygen-bearing low-concentration coal mine methane by the electrochemical catalysis of SOFC anode: From pollutant to clean energy. *Appl Catal B*: *Environ* 2020, **268**: 118413.

[5] Yang L, Zuo CD, Wang SZ, *et al*. A novel composite cathode for low-temperature SOFCs based on oxide proton conductors. *Adv Mater* 2008, **20**: 3280–3283.

[6] Yang Y, Bao H, Ni H, *et al*. A novel facile strategy to suppress Sr segregation for high-entropy stabilized

$La_{0.8}Sr_{0.2}MnO_{3-\delta}$ cathode. *J Power Sources* 2021, **482**: 228959.

[7] Shao ZP, Haile SM. A high-performance cathode for the next generation of solid-oxide fuel cells. *Nature* 2004, **431**: 170–173.

[8] Tarutin AP, Lyagaeva JG, Medvedev DA, *et al*. Recent advances in layered $Ln_2NiO_{4+\delta}$ nickelates: Fundamentals and prospects of their applications in protonic ceramic fuel and electrolysis cells. *J Mater Chem A* 2021, **9**: 154–195.

[9] Dong FF, Chen DJ, Ran R, *et al*. A comparative study of $Sm_{0.5}Sr_{0.5}MO_{3-\delta}$ (M = Co and Mn) as oxygen reduction electrodes for solid oxide fuel cells. *Int J Hydrog Energy* 2012, **37**: 4377–4387.

[10] Nie LF, Liu MF, Zhang YJ, *et al*. $La_{0.6}Sr_{0.4}Co_{0.2}Fe_{0.8}O_{3-\delta}$ cathodes infiltrated with samarium-doped cerium oxide for solid oxide fuel cells. *J Power Sources* 2010, **195**: 4704–4708.

[11] Zhou W, Shao ZP, Ran R, *et al*. A novel efficient oxide electrode for electrocatalytic oxygen reduction at 400–600 ℃. *Chem Commun* 2008: 5791–5793.

[12] Leng YJ, Chan SH, Liu QL. Development of LSCF–GDC composite cathodes for low-temperature solid oxide fuel cells with thin film GDC electrolyte. *Int J Hydrog Energy* 2008, **33**: 3808–3817.

[13] Xia CR, Rauch W, Chen FL, *et al*. $Sm_{0.5}Sr_{0.5}CoO_3$ cathodes for low-temperature SOFCs. *Solid State Ion* 2002, **149**: 11–19.

[14] Xu X, Xu YS, Ma JM, *et al*. Tailoring electronic structure of perovskite cathode for proton-conducting solid oxide fuel cells with high performance. *J Power Sources* 2021, **489**: 229486.

[15] Nirala G, Yadav D, Upadhyay S. Ruddlesden–Popper phase A_2BO_4 oxides: Recent studies on structure, electrical, dielectric, and optical properties. *J Adv Ceram* 2020, **9**: 129–148.

[16] Beppu K, Hosokawa S, Teramura K, *et al*. Oxygen storage capacity of $Sr_3Fe_2O_{7-\delta}$ having high structural stability. *J Mater Chem A* 2015, **3**: 13540–13545.

[17] Yashima M, Enoki M, Wakita T, *et al*. Structural disorder and diffusional pathway of oxide ions in a doped Pr_2NiO_4-based mixed conductor. *J Am Chem Soc* 2008, **130**: 2762–2763.

[18] Tarancón A, Skinner SJ, Chater RJ, *et al*. Layered perovskites as promising cathodes for intermediate temperature solid oxide fuel cells. *J Mater Chem* 2007, **17**: 3175–3181.

[19] Patrakeev MV, Leonidov IA, Kozhevnikov VL, *et al*. Ion-electron transport in strontium ferrites: Relationships with structural features and stability. *Solid State Sci* 2004, **6**: 907–913.

[20] Ling Y, Wang F, Budiman RA, *et al*. Oxygen nonstoichiometry, the defect equilibrium model and thermodynamic quantities of the Ruddlesden–Popper oxide $Sr_3Fe_2O_{7-\delta}$. *Phys Chem Chem Phys* 2015, **17**: 7489–7497.

[21] Wang ZQ, Yang WQ, Shafi SP, *et al*. A high performance cathode for proton conducting solid oxide fuel cells. *J Mater Chem A* 2015, **3**: 8405–8412.

[22] Ling YH, Guo TM, Zhang XZ, *et al*. Evaluation of electrical conductivity and oxygen diffusivity of the typical Ruddlesden–Popper oxide $Sr_3Fe_2O_{7-\delta}$. *Ceram Int* 2017, **43**: 16264–16269.

[23] Mogni L, Prado F, Ascolani H, *et al*. Synthesis, crystal chemistry and physical properties of the Ruddlesden–Popper phases $Sr_3Fe_{2-x}Ni_xO_{7-\delta}$ ($0 \leqslant x \leqslant 1.0$). *J Solid State Chem* 2005, **178**: 1559–1568.

[24] Mogni L, Prado F, Caneiro A. Defect structure and electrical conductivity of the Ruddlesden−Popper phases $Sr_3FeMO_{6+\delta}$ (M = Co, Ni). *Chem Mater* 2006, **18**: 4163–4170.

[25] Ling YH, Wang F, Okamoto Y, *et al*. Oxygen nonstoichiometry and thermodynamic quantities in the Ruddlesden–Popper oxides $La_xSr_{3-x}Fe_2O_{7-\delta}$. *Solid State Ion* 2016, **288**: 298–302.

[26] Ling YH, Wang F, Okamoto Y, *et al*. Oxygen nonstoichiometry and thermodynamic explanation of large oxygen-deficient ruddlesden-popper oxides $La_xSr_{3-x}Fe_2O_{7-\delta}$. *J Am Ceram Soc* 2016, **99**: 3792–3801.

[27] Yoo S, Choi S, Shin J, *et al*. Electrical properties, thermodynamic behavior, and defect analysis of $La_{n+1}Ni_nO_{3n+1+d}$ infiltrated into YSZ scaffolds as cathodes for intermediate-temperature SOFCs. *RSC Adv* 2012, **2**: 4648–4655.

[28] Amow G, Davidson IJ, Skinner SJ. A comparative study of the Ruddlesden–Popper series, $La_{n+1}Ni_nO_{3n+1}$ (*n* = 1, 2 and 3), for solid-oxide fuel-cell cathode applications. *Solid State Ion* 2006, **177**: 1205–1210.

[29] Chen ZZ, Wang JL, Huan DM, *et al*. Tailoring the activity via cobalt doping of a two-layer Ruddlesden–Popper phase cathode for intermediate temperature solid oxide fuel cells. *J Power Sources* 2017, **371**: 41–47.

[30] Yang Y, Chen YH, Tian D, *et al*. A new A-site excessive strategy to improve performance of layered perovskite cathode for intermediate-temperature solid oxide fuel cells. *Electrochimica Acta* 2017, **231**: 686–693.

[31] Velázquez-Palenzuela A, Zhang L, Wang LC, *et al*. Carbon-supported Fe–N_x catalysts synthesized by pyrolysis of the Fe(II)–2,3,5,6-tetra(2-pyridyl)pyrazine complex: Structure, electrochemical properties, and oxygen reduction reaction activity. *J Phys Chem C* 2011, **115**: 12929–12940.

[32] Xiao GL, Liu Q, Wang SW, *et al*. Synthesis and characterization of Mo-doped $SrFeO_{3-\delta}$ as cathode materials for solid oxide fuel cells. *J Power Sources* 2012, **202**: 63–69.

[33] Dai NN, Feng J, Wang ZH, *et al*. Synthesis and characterization of B-site Ni-doped perovskites $Sr_2Fe_{1.5-x}Ni_xMo_{0.5}O_{6-\delta}$ (*x* = 0, 0.05, 0.1, 0.2, 0.4) as cathodes for SOFCs. *J Mater Chem A* 2013, **1**: 14147–14153.

[34] Kang HW, Lim SN, Park SB. Co-doping schemes to enhance H_2 evolution under visible light irradiation over $SrTiO_3$:Ni/M (M = La or Ta) prepared by spray pyrolysis.

Int J Hydrog Energy 2012, **37**: 5540–5549.

[35] Lu YX, Jiang Y, Yang Z, *et al*. Polymer-assisted synthesis of LiNi$_{2/3}$Mn$_{1/3}$O$_2$ cathode material with enhanced electrochemical performance. *J Alloys Compd* 2013, **559**: 203–208.

[36] Sun WP, Shi Z, Fang SM, *et al*. A high performance BaZr$_{0.1}$Ce$_{0.7}$Y$_{0.2}$O$_{3-\delta}$-based solid oxide fuel cell with a cobalt-free Ba$_{0.5}$Sr$_{0.5}$FeO$_{3-\delta}$–Ce$_{0.8}$Sm$_{0.2}$O$_{2-\delta}$ composite cathode. *Int J Hydrog Energy* 2010, **35**: 7925–7929.

[37] Fuoss RM, Kirkwood JG. Electrical properties of solids. VIII. Dipole moments in polyvinyl chloride-diphenyl systems. *J Am Chem Soc* 1941, **63**: 385–394.

[38] Shi N, Su F, Huan DM, *et al*. Performance and DRT analysis of P-SOFCs fabricated using new phase inversion combined tape casting technology. *J Mater Chem A* 2017, **5**: 19664–19671.

[39] Xu H, Dang Z. Numerical investigation of coupled mass transport and electrochemical reactions in porous SOFC anode microstructure. *Int J Heat Mass Transf* 2017, **109**: 1252–1260.

[40] Wang X, Ma Z, Zhang T, *et al*. Charge-transfer modeling and polarization DRT analysis of proton ceramics fuel cells based on mixed conductive electrolyte with the modified anode-electrolyte interface. *ACS Appl Mater Inter* 2018, **10**: 35047–35059.